STRUCTURAL BIOLOGY

ISSN: 2059-7983
journals.iucr.org/d

Structural visualization of transient interactions between the *cis*-acting acyltransferase and acyl carrier protein of the salinomycin modular polyketide synthase

Y. Feng, F. Zhang, S. Huang, Z. Deng, L. Bai and J. Zheng

Acta Cryst. (2022). D**78**, 779–791

STRUCTURAL BIOLOGY

ISSN 2059-7983

Structural visualization of transient interactions between the *cis*-acting acyltransferase and acyl carrier protein of the salinomycin modular polyketide synthase

Y. Feng,[a] F. Zhang,[a] S. Huang,[a] Z. Deng,[a] L. Bai[a] and J. Zheng[a,b]*

[a]State Key Laboratory of Microbial Metabolism, School of Life Sciences and Biotechnology, Shanghai Jiao Tong University, 800 Dongchuan Road, Minhang District, Shanghai 200240, People's Republic of China, and [b]Joint International Research Laboratory of Metabolic and Developmental Sciences, Shanghai Jiao Tong University, Shanghai, People's Republic of China. *Correspondence e-mail: jtzheng@sjtu.edu.cn

Received 23 November 2021
Accepted 2 May 2022

Edited by B. Kobe, University of Queensland, Australia

Keywords: salinomycin modular polyketide synthases; polyketides; protein–protein interactions; acyltransferases; acyl carrier proteins; cross-linking.

PDB references: SalAT9, 7vt1; SalAT9M–ACP9, 7vrs

Supporting information: this article has supporting information at journals.iucr.org/d

Transient protein–protein interactions between *cis*-acting acyltransferase (AT) and acyl carrier protein (ACP) domains are critical for the catalysis and processivity of modular polyketide synthases (mPKSs), but are challenging for structural characterization due to the intrinsically weak binding affinity. Here, a stable complex of *cis*-acting AT and ACP domains from the ninth module of the salinomycin mPKS was obtained using a maleimide cross-linker and the structure of the complex was determined at 2.6 Å resolution. The crystal structure shows that the AT in combination with the ketosynthase (KS)-to-AT linker forms a C-shaped architecture to embrace the ACP. The large hydrolase subdomain of the AT serves as a major binding platform for the ACP, while the small ferredoxin-like subdomain of the AT and the KS-to-AT linker cooperate with each other to constrain binding of the ACP. The importance of interface residues in *cis*-acting AT–ACP interactions was confirmed by mutagenesis assays. The interaction mode observed in the *cis*-acting AT–ACP complex is completely different from those observed in *trans*-acting AT–ACP complexes, where the ACP primarily contacts the small domain of the AT. The complex structure provides detailed mechanistic insights into AT–ACP recognition in *cis*-AT mPKSs.

1. Introduction

Polyketides, such as erythromycin, avermectin and rifamycin, are a large group of clinically important natural products (Nivina *et al.*, 2019; Klaus & Grininger, 2018). Although structurally diverse, they are synthesized by polyketide synthases (PKSs) from relatively simple short-chain carboxylic acids activated by coenzyme A (CoA) and, to a lesser degree, standalone acyl carrier proteins (ACPs). The assembly of a polyketide chain is similar to that of a fatty-acid chain. Usually, a monocarboxylic acid is utilized as a starter unit and is condensed with dicarboxylic acid extender units iteratively until the polyketide chain reaches an appropriate length. The selection of various starter and extender units by an acyltransferase (AT) is the first step of polyketide chain extension. The AT loads an acyl unit onto the phosphopantetheine thiol of an ACP domain, where it is used in the decarboxylative Claisen condensation catalyzed by a ketosynthase (KS) to elongate the polyketide chain, followed by optional modifying reactions using ketoreductase (KR), dehydratase (DH) and enoylreductase (ER) enzymes. According to the architectural organization of catalytic enzymes, PKSs are divided into different groups. Modular PKSs (mPKSs) containing covalently fused domains for catalytic cycles are among the most

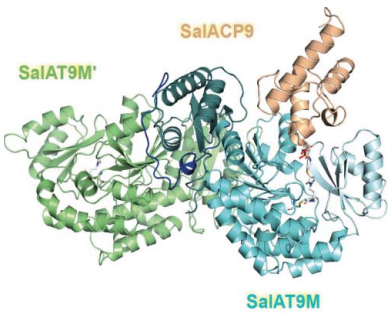

versatile megaenzymes, each module of which is responsible for a single round of polyketide chain elongation, minimally consisting of a KS, an AT and an ACP. Canonical mPKSs contain a *cis*-acting AT domain (*cis*-AT) in every module (Dodge *et al.*, 2018). However, mPKSs that have modules without embedded AT domains have also been discovered and utilize external *trans*-acting ATs (*trans*-ATs), which are standalone enzymes, to provide acyl units for polyketide chain elongation (Kosol *et al.*, 2018).

The apparent architectural modularity encourages the construction of hybrid mPKSs to generate unnatural polyketides. The *cis*-AT domains control the acyl unit incorporated into every elongation step and therefore are attractive engineering targets (Kalkreuter *et al.*, 2019; Koryakina *et al.*, 2017; Bravo-Rodriguez *et al.*, 2015; Li *et al.*, 2018). Swapping *cis*-AT domains is a useful approach to regiospecifically incorporate diverse types of starter and extender units into polyketides to obtain biologically active analogs. Examples of the successful engineering of mPKSs by swapping *cis*-AT domains have been reported; however, reduced or abolished production of polyketide analogs are also observed (Yuzawa *et al.*, 2017, 2018). Recent evidence indicates that proper *cis*-AT–ACP recognition is critical to the recruitment of acyl units during chain elongation (Dodge *et al.*, 2018). Representative *cis*-AT domains of 6-deoxyerythronolide B synthase (DEBS), a typical mPKS, prefer the cognate ACP domain partner by a factor of ∼20 in k_{cat}/K_m over ACP domains from other modules of the same synthase, suggesting that specific *cis*-AT–ACP interactions are important for kinetically efficient transacylation reactions catalyzed by *cis*-AT domains in polyketide chain elongation (Dunn *et al.*, 2013). This highlights the need for a more careful consideration of proper protein–protein interactions in engineering mPKSs. In contrast, *trans*-ATs have a good tolerance for unnatural ACP partners. The *trans*-AT from disorazole synthase (DSZS AT) exhibits a strict specificity toward malonyl-CoA, but is considerably promiscuous with respect to ACP partners, tolerating of a range of noncognate ACPs (Dunn *et al.*, 2014). The k_{cat}/K_m values for DSZS AT with two DEBS ACP domains are greater than that for DEBS *cis*-AT3 with its cognate DEBS ACP3 partner.

The inherently transient and weak nature of the interaction is the key challenge in understanding protein–protein interactions between AT and ACP. The weak mutual binding affinity hampers the structural determination of an AT–ACP complex to directly visualize the protein–protein interactions. Wong and coworkers introduced a cysteine mutation at the catalytic Ser86 of DSZS AT and then used this S86C mutant for cross-linking to the 4′-phosphopantetheine of the ACP1 partner using bifunctional electrophilic reagents (Wong *et al.*, 2011). A stable DSZS *trans*-AT–ACP1 complex was obtained, but the yield of the resulting complex was not sufficient for crystallization trials. Eguchi and coworkers obtained sufficient DSZS *trans*-AT–ACP1 complex by using a synthetic pantetheineamide as the cross-linking agent, which enabled structural determination of the DSZS *trans*-AT–ACP1 complex (Miyanaga *et al.*, 2018). The bifunctional maleimide reagent BMOE has successfully been used to trap the transient complex of the *trans*-AT VinK and the standalone ACP VinL from the vicenistatin pathway for structural characterization (Miyanaga *et al.*, 2016). These complex structures provide detailed molecular insights into how *trans*-ATs recognize their ACP partners. During the preparation of this manuscript, structures of *cis*-AT PKS modules were reported (Bagde *et al.*, 2021; Cogan *et al.*, 2021). The X-ray structure of Lsd14 shows the transacylation state of apo LsdACP7. Detailed understanding of *cis*-AT–ACP interactions is important in order to engineer *cis*-AT modular PKSs to regiospecifically incorporate acyl units into polyketides.

Salinomycin, which has antibacterial and anticoccidial activities, is an important commercial polyether polyketide that is widely used as a food additive in animal husbandry. Its mPKS comprises a loading module and 14 extension modules, each of which contains a *cis*-AT domain (Jiang *et al.*, 2012). Here, we report the crystal structure of a *cis*-AT–ACP complex from the ninth extension module of salinomycin PKS. The transient *cis*-AT–ACP complex was obtained using 1,4-bis(maleimido)butane (BMB) as a cross-linking agent. The ACP-binding mode in the *cis*-AT–ACP complex structure is strikingly different from those of previously reported *trans*-AT–ACP complex structures. The ACP primarily contacts the large subdomain of the AT in the structure of the *cis*-AT–ACP complex, whereas the ACP primarily contacts the small domain of the AT in the *trans*-AT–ACP complex structures (Miyanaga *et al.*, 2016, 2018). The binding mode of SalACP9 to SalAT9 also differs from that observed in the modular structure of Lsd14. The complex structure provides detailed mechanistic insights into the protein–protein interactions between the AT and ACP domains of *cis*-AT mPKSs.

2. Methods

2.1. Plasmids

All primers used for PCR reactions are listed in Supplementary Table S1. Genomic DNA of *Streptomyces albus* XM211 was used as a template (Jiang *et al.*, 2012). The DNA fragments were inserted into the pET-28a vector via NdeI and EcoRI restriction sites to obtain pET028a-*sal*AT9 and pET028a-*sal*ACP9, respectively. All plasmids were verified by sequencing.

2.2. Site-directed mutagenesis

The mutants were generated using the GeneTailor Site-Directed Mutagenesis System following the manufacturer's instructions. The oligonucleotides used for mutagenesis are listed in Supplementary Table S1.

2.3. Purification of SalAT9 and its mutants

The N-terminally His_6-tagged recombinant SalAT9 protein was expressed in *Escherichia coli* BL21(DE3) cells cultured in LB broth. Cells were grown in the presence of 50 mg l^{-1} kanamycin, induced with 0.35 m*M* isopropyl *β*-D-1-thio-galactopyranoside at an OD_{600} of 0.6 and incubated at 16°C

for 12 h. The cells were harvested by centrifugation and were resuspended in lysis buffer consisting of 500 m*M* NaCl, 50 m*M* Tris pH 7.0, 10%(*v*/*v*) glycerol. The pelleted cells were lysed by sonication (10 s pulses for 10 min) followed by centrifugation at 15 000*g* for 40 min to remove debris. The protein was loaded onto nickel–NTA resin (Smart-Life Sciences), washed with 50 ml lysis buffer containing 30 m*M* imidazole and eluted with lysis buffer containing 250 m*M* imidazole. For enzymatic assays and cross-linking reactions, the purified SalAT9 was further polished by size-exclusion chromatography (SEC) using a Superdex 200 column (GE Healthcare Life Sciences) equilibrated with buffer consisting of 10 m*M* Tris, 150 m*M* NaCl pH 7.0, 10%(*v*/*v*) glycerol. The eluted protein was collected, concentrated to a concentration of ∼10 mg ml^{-1} using Amicon Ultra Centrifugal Filters (Millipore Sigma) with a 10 kDa molecular-weight cutoff and stored at −80°C. The SalAT9 mutants were purified using similar protocols.

2.4. SalACP9 purification

Holo SalACP9 was expressed in *E. coli* BAP1 with the 4′-phosphopantetheinyl transferase gene *sfp* from *Bacillus subtilis* integrated into its chromosome (Pfeifer *et al.*, 2001), purified using nickel–NTA resin as described above and polished using a Superdex 75 column (GE Healthcare Life Sciences) equilibrated with buffer consisting of 10 m*M* Tris, 150 m*M* NaCl pH 7.0, 10%(*v*/*v*) glycerol. The resulting protein was collected and concentrated to a concentration of ∼10 mg ml^{-1} using Amicon Ultra Centrifugal Filters with 3 kDa molecular-weight cutoff.

2.5. Kinetic analysis

The release of CoA catalyzed by SalAT9 and its mutants was coupled to the generation of NADH, which can be monitored spectrophotometrically at 340 nm (Dunn *et al.*, 2013). Reactions were implemented at 25°C in 100 µl 50 m*M* sodium phosphate buffer pH 7.5 containing 1 µ*M* AT, 3.125–100 µ*M* ethylmalonyl-CoA, 0.4 mU µl^{-1} α-ketoglutarate dehydrogenase (αKGDH), 1 m*M* EDTA, 0.05 mg ml^{-1} *N*,*O*-bis-(trimethylsilyl)acetamide, 1 m*M* tris(2-carboxyethyl)-phosphine (TCEP), 0.4 m*M* NAD^+, 0.4 m*M* thiamine pyrophosphate (TPP), 2 m*M* α-ketoglutaric acid and 10% glycerol. 100 µ*M* SalACP9 was supplemented to assay AT-catalyzed transacylation reactions. Kinetic parameters were deduced by nonlinear regression analysis based on Michaelis−Menten kinetics.

2.6. Ellman's assay

The thiol group of holo SalACP9 and its mutants was detected using Ellman's assay (Riener *et al.*, 2002). The Ellman's reagent 5,5′-dithio-bis-2-nitrobenzoic acid (DTNB) was prepared as a 2.5 m*M* solution in 0.1 *M* phosphate buffer pH 8.0 containing 1.0 m*M* EDTA. 50 µ*M* ACP was mixed with 500 µ*M* DTNB in 100 µl reaction buffer [10 m*M* Tris, 150 m*M* NaCl pH 7.0, 10%(*v*/*v*) glycerol] for 5 min at room temperature. The absorbance of the reaction mixture at 412 nm was detected. The apparent absorbance of a blank containing protein buffer in the absence of DTNB was subtracted from the measured values. The thiol concentration was determined from the absorbance of NTB^{2-} using an absorption coefficient of 13 600 M^{-1} cm^{-1}. All experiments were carried out in triplicate. The ratio of free thiol is equal to the thiol concentration divided by the ACP concentration.

2.7. Comparing the efficiency of cross-linkers

For AT–ACP cross-linking trials, 100 µ*M* AT was mixed with 500 µ*M* cross-linkers (Thermo Fisher Scientific) of differing lengths in 20 µl reaction buffer for 2 h at 4°C, followed by the addition of 500 µ*M* ACP to initialize the cross-linking reaction. After 3 h, SDS–PAGE loading buffer was added to quench the reaction and SDS–PAGE was used to detect the results of the cross-linking reaction. *ImageJ* was used to assay each band to estimate the amounts of AT and AT–ACP. The cross-linking efficiency was calculated as AT–ACP/(AT–ACP + AT) × 100.

2.8. Preparing the AT–ACP complex

The AT mutant (S190C/C298S/C347S) eluted from nickel–NTA resin was incubated with BMB dissolved in DMSO (five equivalents) for 2 h at 4°C. The modified protein was purified by SEC using a HiLoad Superdex 200 column (GE Healthcare Life Sciences). The eluted protein was collected and concentrated to ∼10 mg ml^{-1}. The His_6 tag was cleaved with bovine thrombin (1 U per milligram of protein) for 16 h at 4°C. The remaining protein with His_6 tag was removed using nickel–NTA resin. The resulting tag-free SalAT9M was concentrated to ∼8 mg ml^{-1}. The tag-free SalAT9M modified by BMB (100 µ*M*) was incubated with 75 µ*M* SalACP9 on ice for 4 h for cross-linking. The resulting complex was purified with nickel–NTA resin using the His_6 tag of the ACP. The eluted complex was further purified by SEC using a HiLoad Superdex 75 column to remove unbound ACP. The complex was collected and concentrated to ∼11 mg ml^{-1}.

2.9. Crystallization, data collection and structure determination

Crystals of SalAT9 were grown from a 2:1 mixture of protein solution (10 mg ml^{-1} in 10 m*M* Tris, 25 m*M* NaCl pH 7.5) and reservoir solution [0.15 *M* DL-malic acid pH 7.0, 20%(*v*/*v*) PEG 3350] by sitting-drop vapor diffusion at 20°C in three weeks. Crystallization of the SalAT9M–ACP9 complex was performed by sitting-drop vapor diffusion at 20°C by mixing 2 µl protein solution (11 mg ml^{-1} in 10 m*M* Tris, 150 m*M* NaCl pH 7.0) with 1 µl reservoir solution. The best crystals were obtained using a solution consisting of 0.1 *M* Tris–HCl pH 8.0, 0.4 *M* $MgCl_2$, 0.2 *M* Na_2SO_4, 26%(*v*/*v*) PEG 3350 within four days.

Before the X-ray diffraction experiment, the crystals were transferred into reservoir solution supplemented with 20%(*v*/*v*) glycerol for cryoprotection and flash-cooled in liquid nitrogen. Data sets for SalAT9 and SalAT9M–ACP9 were collected on beamlines BL18U1 and BL19U1 at Shanghai Synchrotron Radiation Facility (SSRF), People's Republic of China. All

diffraction data were processed using the *HKL*-2000 package. The structure of SalAT9 was determined by the molecular-replacement method with *Phaser* from the *CCP*4 suite (Winn *et al.*, 2011) using the coordinates of SalAT14 (PDB entry 6iyt; Zhang *et al.*, 2019). The structure of the SalAT9M–ACP9 complex was determined by the molecular-replacement method using SalAT9 as the search model. SalACP9 was manually built in *Coot* (Emsley *et al.*, 2010). The ligand was adjusted with *Coot* (Debreczeni & Emsley, 2012). Both structures were refined using *REFMAC* (Murshudov *et al.*, 2011). The rotation between subdomains was calculated using *PyMOL*. The interface area between protein molucules was calculated using the *PISA* server (Schlee *et al.*, 2019).

2.10. Docking models of SalAT9 and SalACP9

The structures of SalAT9 and SalACP9 were taken from the SalAT9M–ACP9 complex. *In silico* docking simulations were performed using *ClusPro* 2.0 (Kozakov *et al.*, 2017) and *RosettaDock*-3.2 (Lyskov & Gray, 2008). For initial simulations in *ClusPro*, SalAT9 and SalACP9 were set as the receptor and ligand, respectively, using default settings. To simulate ACP docking to AT, a maximum distance restraint of 25 Å was used between the SalAT9M and SalACP9 catalytic serine residues, and the distance between Arg399 of SalAT9M and Asp46 of SalACP9 was restricted to 1–5 Å. The first ten docked models were judged manually according to the binding free energy calculated by *FoldX* 5.0 (Delgado *et al.*, 2019). The best model from *ClusPro* was used as a decoy model for *RosettaDock* simulations. The ideal docked model was identified by interface score and total score.

3. Results

3.1. Trapping the AT–ACP complex by cross-linking

The ninth module of the salinomycin mPKS has a typical KS–AT–KR–ACP domain organization and recruits an

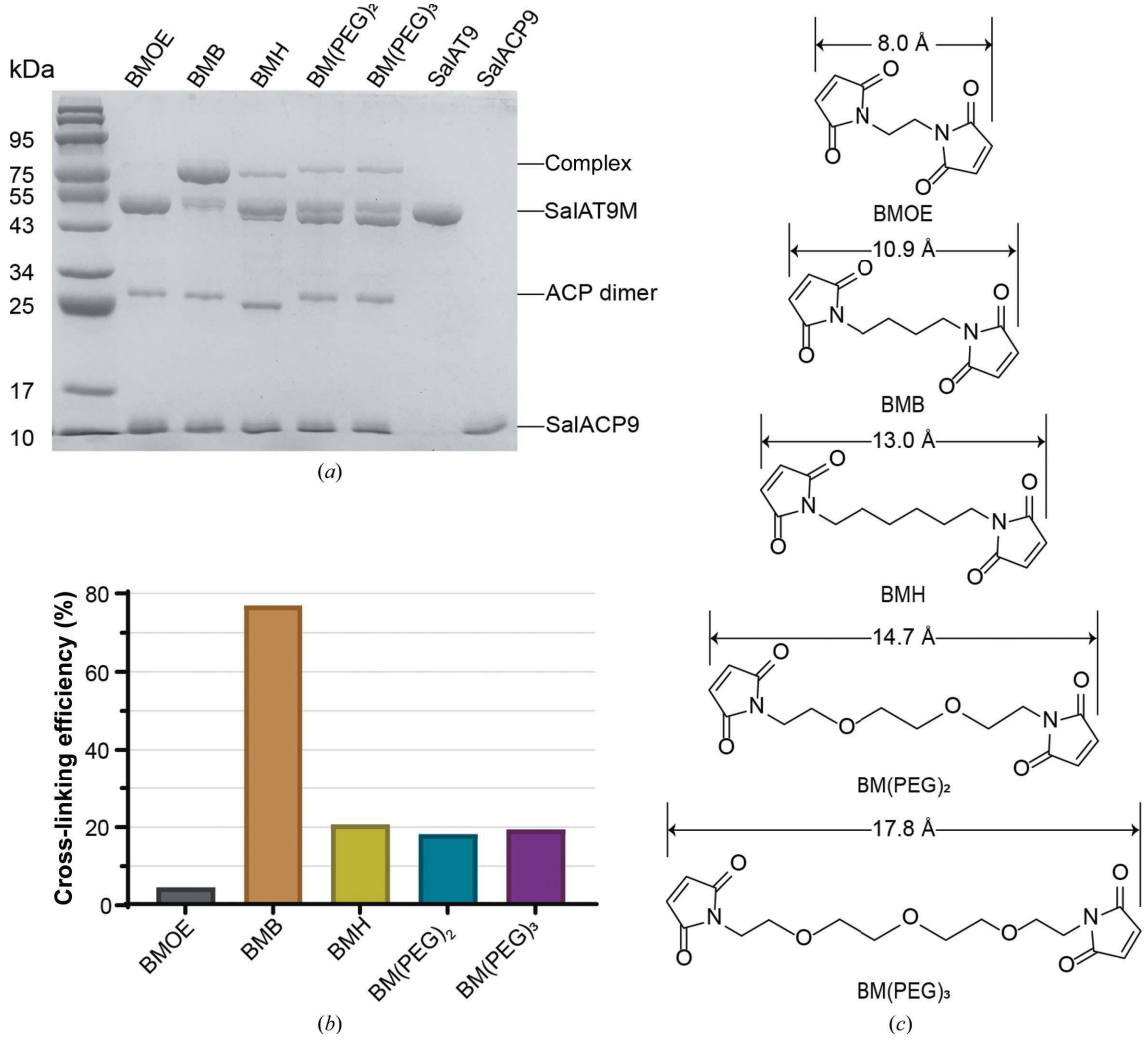

Figure 1
Cross-linking reaction of SalAT9M and SalACP9. (*a*) BMB demonstrated the highest cross-linking efficiency. Covalent cross-linking between SalAT9M (~49 kDa) and SalACP9 (~11 kDa) results in the SalAT9M–ACP9 complex (~60 kDa). Dimeric SalACP9 (~22 kDa) was also formed. (*b*) Cross-linking efficiency of various cross-linkers. *ImageJ* was used to assay each band to estimate the amount of AT and AT–ACP. The cross-linking efficiency was calculated as AT–ACP/(AT–ACP + AT) × 100. (*c*) The cross-linkers used in the reactions.

Table 1
Data-collection and refinement statistics (molecular replacement).

	SalAT–ACP9	AT9
Data collection		
Wavelength (Å)	0.97853	0.97778
Space group	$P222_1$	$P2_12_12_1$
a, b, c (Å)	75.6, 102.1, 151.0	65.2, 102.6, 134.2
Resolution (Å)	50.00–2.60	50.00–2.50
R_{merge}	0.136 (0.620)	0.086 (0.841)
$\langle I/\sigma(I)\rangle$	12.6 (3.7)	22.6 (2.2)
Completeness (%)	99.8 (99.6)	99.7 (89.7)
Multiplicity	6.2 (6.1)	6.5 (5.9)
Refinement statistics		
Resolution (Å)	50–2.60	50–2.50
Unique reflections	34508	29843
R_{work}/R_{free}	0.19/0.23	0.22/0.25
No. of atoms		
Protein	7161	6355
Water	119	17
PNS	21	
ME9	36	
B factors (Å^2)		
Protein	45	42
Water	34	25
PNS	62	
ME9	59	
R.m.s.d. (Å)		
Bond lengths (Å)	0.008	0.007
Bond angles (°)	1.414	1.414

ethylmalonyl-CoA extender unit (Supplementary Fig. S1). To assay the interactions between the *cis*-AT and ACP domains, SalAT9 (residues 2583–3027 of SlnA5), which encompasses the entire AT domain and the adjacent KS-to-AT linker domain, and SalACP9 (residues 3585–3670 of SlnA5) were overexpressed and purified to homogeneity. Both SalAT9 and SalACP9 exist as monomers in solution (Supplementary Fig. S2). SalACP9 was expressed in *E. coli* BAP1 with the 4′-phosphopantetheinyl transferase gene *sfp* from *B. subtilis* integrated into its chromosome to ensure post-translational modification of the active-site serine (Pfeifer *et al.*, 2001). The transacylation activity of the standalone SalAT9 was confirmed using ethylmalonyl-CoA and SalACP9 as substrates (Supplementary Fig. S3).

Bis(maleimido)ethane (BMOE) was first investigated for use in the cross-linking reaction of SalAT9 and SalACP9 due to its success in structural determination of the VinK–VinL complex (Miyanaga *et al.*, 2016). Cross-linking was observed between wild-type SalAT9 and SalACP9 (Supplementary Fig. S4). BMB and bis(maleimido)hexane (BMH) also resulted in undesired cross-linking reactions. Mutating Cys298 and Cys347 of SalAT9 to serine residues abolished the cross-linking reactions occurring at undesired positions. The double mutant was almost as active as the wild-type enzyme in the transacylation reactions (Supplementary Fig. S3). We introduced a cysteine mutation at the position of Ser190 into the double mutant of SalAT9, which corresponds to the catalytic Ser86 of DSZS AT that was mutated to cysteine in the cross-linking experiment (Supplementary Fig. S5; Wong *et al.*, 2011), and then used the triple mutant (named SalAT9M) in the subsequent cross-linking reaction. We compared the crosslinking efficiencies of bismaleimide cross-linkers of differing lengths, including BMOE, BMB, BMH, 1,8-bis-maleimido-diethyleneglycol [BM(PEG)$_2$] and 1,11-bismale-imido-triethyleneglycol) [BM(PEG)$_3$] (Fig. 1), in preparing the SalAT9M–ACP9 complex. BMB demonstrated the highest cross-linking efficiency and was chosen for the large-scale preparation of the SalAT9M–ACP9 complex (Fig. 1*b*). There are no cysteines in SalACP9, suggesting that specific cross-linking occurs between Cys190 of SalAT9M and the 4′-phos-phopantetheine of SalACP9. Cross-linking between two SalACP9 molecules was observed (Fig. 1*a*). To eliminate this undesired cross-linking reaction, SalAT9M was first incubated with BMB, followed by the removal of excess BMB (Supple-mentary Fig. S6). SalAT9M modified by BMB was incubated with thrombin to remove the N-terminal His tag and was then reacted with SalACP9 to obtain the covalent complex. The resulting complex was separated from the reaction using the affinity tag of SalACP9 and polished by size-exclusion chro-matography. The resulting SalAT9M–ACP9 complex exists as a monomer in solution (Supplementary Fig. S2).

3.2. Overall structure of the AT–ACP complex

A large-scale cross-linking reaction was performed to prepare the SalAT9M–ACP9 complex for crystallization trials. Crystals were reproducibly obtained by the sitting-drop method from the complex purified to homogeneity. After optimization of the crystallization conditions, we determined the crystal structure of the SalAT9M–ACP9 complex by molecular replacement at 2.6 Å resolution in space group $P222_1$, with R_{work} and R_{free} values of 0.19 and 0.23, respectively (Table 1). A SalAT9M–ACP9 complex and a standalone SalAT9M molecule were observed in the crystallographic asymmetric unit (Fig. 2). The electron density shows that S190C of the standalone SalAT9M is modified by a BMB molecule, whereas density for the phosphopantetheine connected to BMB is barely visible (Supplementary Fig. S7). As shown in Supplementary Fig. S2(*b*), there is negligible standalone SalAT9M in the complex prepared for crystal-lization. These results suggests that the ACP is likely to be degraded during the crystallization process.

The SalAT9M–ACP9 complex structure shows that the AT, in combination with the KS-to-AT linker, forms a C-shaped architecture to embrace the ACP (Fig. 2*b*). Electron density for 4′-phosphopantetheine and the BMB cross-linking reagent is clearly observed in the substrate-binding tunnel of SalAT9M. The 4′-phosphopantetheine is covalently attached to Ser47 of the ACP. The BMB maleimide groups covalently connect the AT and ACP by attaching to both the side-chain sulfhydryl group of Cys190 of SalAT9M and the terminal sulfhydryl group of the 4′-phosphopantetheine of SalACP9 (Fig. 2*c*). The conformation observed in the complex structure is mechanistically reasonable for delivering the acyl group into the active site to initiate the transacylation reaction.

SalAT9 is organized into a large α,β-hydrolase subdomain (residues 97–224 and 299–418) and a small ferredoxin-like subdomain (residues 228–294) (Fig. 2*b*). The N-terminal KS-to-AT linker (residues 1–92) forms a three-stranded anti-

parallel β-sheet and three α-helices packing against the AT domain. The overall architecture of SalAT9 is similar to our previously reported structures of SalAT2 (PDB entry 6iyo; 1.7 Å r.m.s.d. for 294 C^{α} atoms; 30% sequence identity), SalAT8 (PDB entry 6iyr; 1.2 Å r.m.s.d. for 364 C^{α} atoms; 29% sequence identity) and SalAT14 (PDB entry 6iyt; 1.0 Å r.m.s.d. for 359 C^{α} atoms; 31% sequence identity) from the same mPKS. SalAT9 is specific for an ethylmalonyl-CoA extender unit and has a VASH motif at the active site, which provides a larger pocket to accommodate the ethyl side chain compared with the corresponding YASH motif specific for methylmalonyl-CoA (Supplementary Fig. S5; Zhang *et al.*, 2019).

The substrate-binding tunnel is formed at the interface of the large and small subdomains (Fig. 2*b*). An electrostatic potential surface indicates that the tunnel is positively charged, facilitating the binding of the negatively charged ethylmalonyl unit (Fig. 2*d*). The 4′-phosphopantetheine and

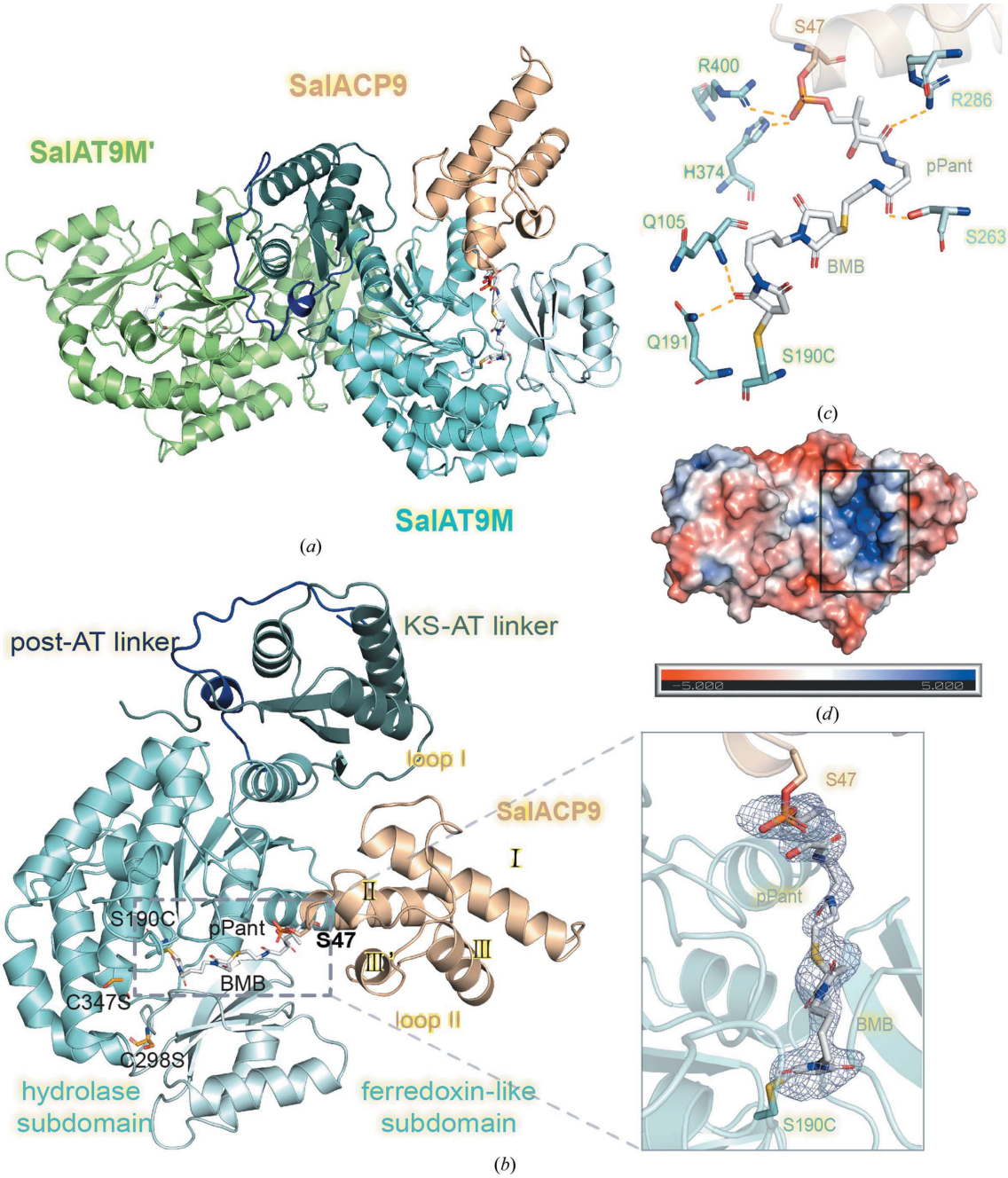

Figure 2
Overall structure of SalAT9M–ACP9. (*a*) A SalAT9M–ACP9 complex and a standalone SalAT9M molecule (named SalAT9M′) were observed. (*b*) The AT, in combination with the KS-to-AT linker, forms a C-shaped architecture to embrace the ACP. Ser47 of SalACP9, 4′-phosphopantetheine (pPant), BMB and Cys190 of SalAT9M are shown as sticks. The insert shows the omit $F_o - F_c$ map of pPant and BMB contoured at 2.5σ. (*c*) Substrate-tunnel residues involved in interactions with pPant and BMB. (*d*) Electrostatic potential of SalAT9M calculated using the *PyMOL APBS* plugin. Colors range from blue (positive) to white (neutral) to red (negative). The substrate-binding tunnel (indicated by a rectangle) is positively charged.

BMB are positioned in the substrate tunnel. The side chain of Arg400 located at the entrance to the SalAT9 substate tunnel forms electrostatic interactions with the phosphate group of the 4′-phosphopantetheine of SalACP9 (Fig. 2*c*). A hydrogen-bond interaction with the phosphate group occurs via the side chain of His374 of SalAT9. The side chain of Arg286 of SalAT9 positioned on the opposite side of the substate tunnel makes a hydrogen bond to the amide carbonyl of the 4′-phosphopantetheine. Ser263 forms a hydrogen bond to the second amine carbonyl O atom of the pantetheine through its side-chain hydroxyl group. The side chain of Gln191 and the backbone of Gln105 make hydrogen bonds to a carbonyl of the maleimide ring. During the transacylation reaction, Gln191 is likely to help in the orientation of the malonyl group (Zhang *et al.*, 2020).

The overall structure of SalACP9 closely resembles its counterparts in the extension modules of the *cis*-AT DEBS (ACP2; PDB entry 2ju1; 1.3 Å r.m.s.d. for 73 C^{α} atoms; 50%

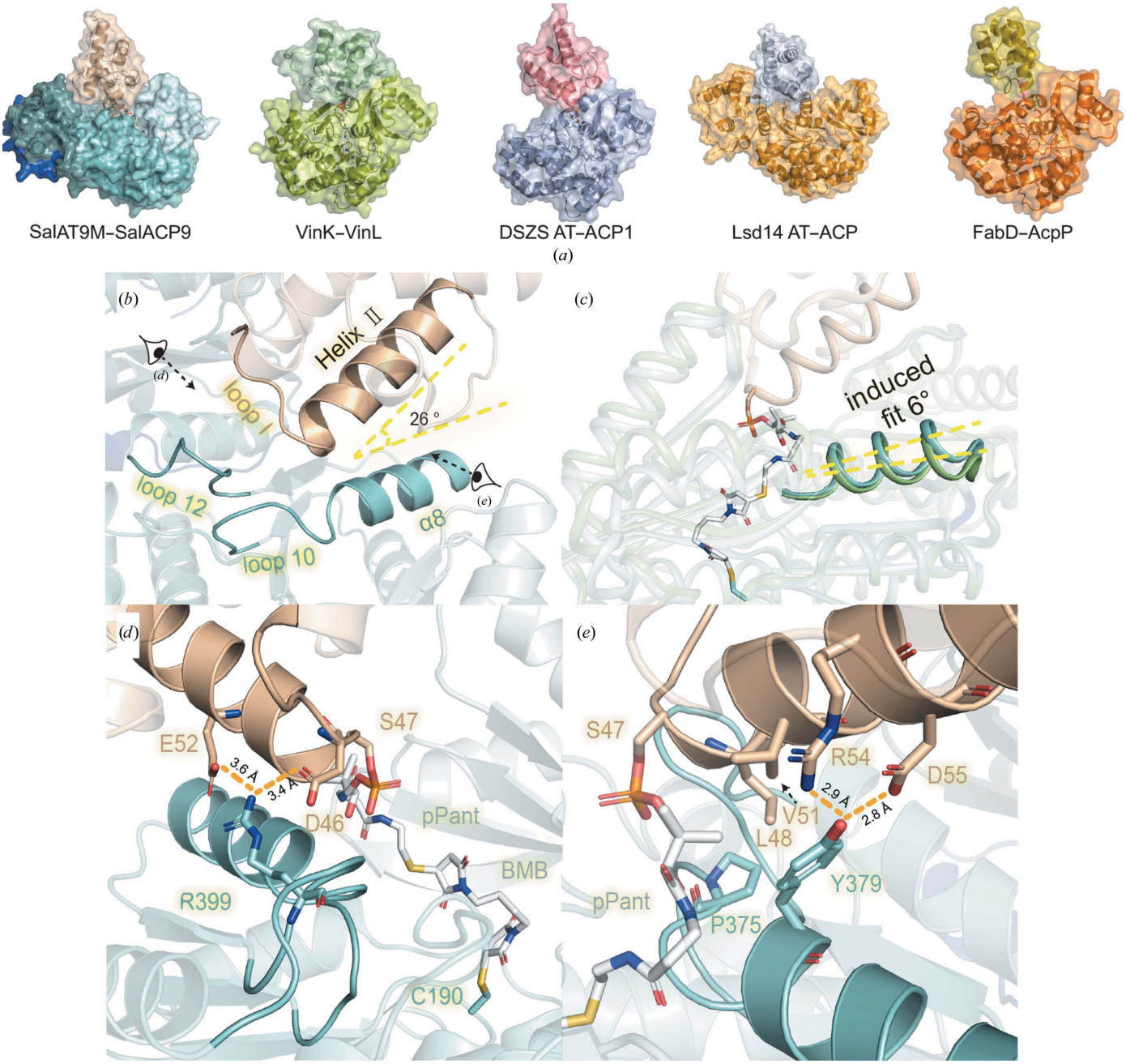

Figure 3
The large hydrolase subdomain of SalAT9M functions as the major binding platform for SalACP9. (*a*) Structures of the SalAT9M–ACP9, VinK–VinL, DSZS AT–ACP1, Lsd14 AT–ACP and FabD–AcpP complexes. (*b*) The αII helix of SalACP9 packs against helix α8, loop 10 and loop 12 of the large hydrolase. The visual orientations of (*d*) and (*e*) are labeled. (*c*) Helix α8 of SalAT9M in the complex structure rotates 6° upon binding SalACP9 compared with the standalone SalAT9M′. (*d*) The positively charged guanidine group of Arg399 located in loop 12 of SalAT9M interacts with Asp46 of the SalACP9 'DSL' motif and Glu52 located in the αII helix. (*e*) Residues involved in interactions between the ACP αII helix and AT helix α8.

sequence identity; Alekseyev *et al.*, 2007) and the ACP1 of the *trans*-AT DSZS (PDB entry 5zk4; 0.9 Å r.m.s.d. for 47 C^{α} atoms; 23% sequence identity; Miyanaga *et al.*, 2018) and the standalone ACP VinL in the vicenistatin pathway (PDB entry 5czd; 3.2 Å r.m.s.d. for 41 C^{α} atoms; 16% sequence identity; Miyanaga *et al.*, 2016). It is composed of three major α-helices (αI, αII and αIII) and two connecting loops (Fig. 2*b*). The three major α-helices form a right-hand twisted bundle that is observed in most known ACP structures. The αI helix is significantly longer and spans the other two helices. A small αIII′ helix in the second loop, almost perpendicularly oriented to the three major α-helices, also contributes to the packing of the twisted bundle. Ser47 carrying the 4′-phosphopantetheine is located at the N-terminus of the αII helix.

3.3. The AT large subdomain serves as a major binding platform for ACP

In the SalAT9M–ACP9 complex structure, the interface between SalAT9 and SalACP9 comprises ∼450 Å^2, representing 9.1% of the surface area of SalACP9 and 2.6% of the surface area of SalAT9. This contact area is smaller than those of previously reported *trans*-AT–ACP complexes such as the VinK–VinL structure (Miyanaga *et al.*, 2016; ∼650 Å^2) and the DSZS AT–ACP1 structure (∼600 Å^2; Miyanaga *et al.*, 2018). It is also smaller than that of the Lsd14 AT–ACP complex (∼610 Å^2; Bagde *et al.*, 2021), but is larger than that of the FabD–AcpP complex (∼350 Å^2; Misson *et al.*, 2020) (Fig. 3). The small contact areas are consistent with the weak and transient nature of the interactions between the AT and ACP partners. SalACP9 primarily contacts the large hydrolase subdomain of SalAT9 by its αII helix (residues 47–61) and the preceding C-terminus of loop I (residues 43–46), whereas the ACP of the *trans*-AT–ACP complex primarily contacts the small domain of AT (Fig. 3*a*). The αII helix of SalACP9 packs against helix α8 (residues 378–388) of the large hydrolase subdomain with an angle of 26° (Fig. 3*b*). Besides helix α8, loop 10 (residue 371–377) and loop 12 (residues 397–404) of SalAT9M are also involved in the major binding platform for SalACP9. The standalone SalAT9M molecule was superposed onto AT in the complex; helix α8 rotates 6° upon SalACP9 binding (Fig. 3*c*). The positively charged guanidine group of

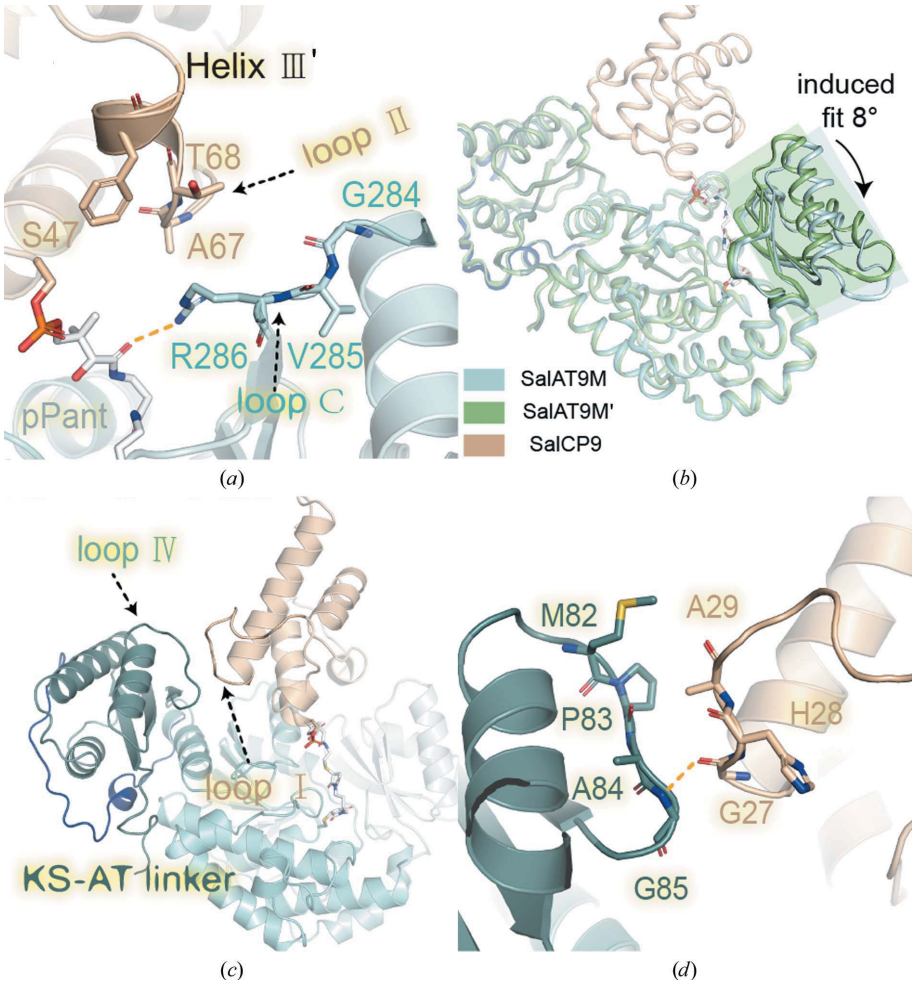

Figure 4
The AT small ferredoxin-like subdomain and KS-to-AT linker constrain ACP binding. (*a*) The short helix αIII′ of loop II of SalACP9 packs against loop C of the small subdomain of SalAT9M. (*b*) SalACP9 binding induces SalAT9M to adopt a more open state compared with the standalone SalAT9M′. (*c*) Loop IV of the KS-to-AT linker makes contacts with the N-terminal residues of loop I of SalACP9. (*d*) Resides involved in the contacts between loop IV of the KS-to-AT linker and loop I of the ACP.

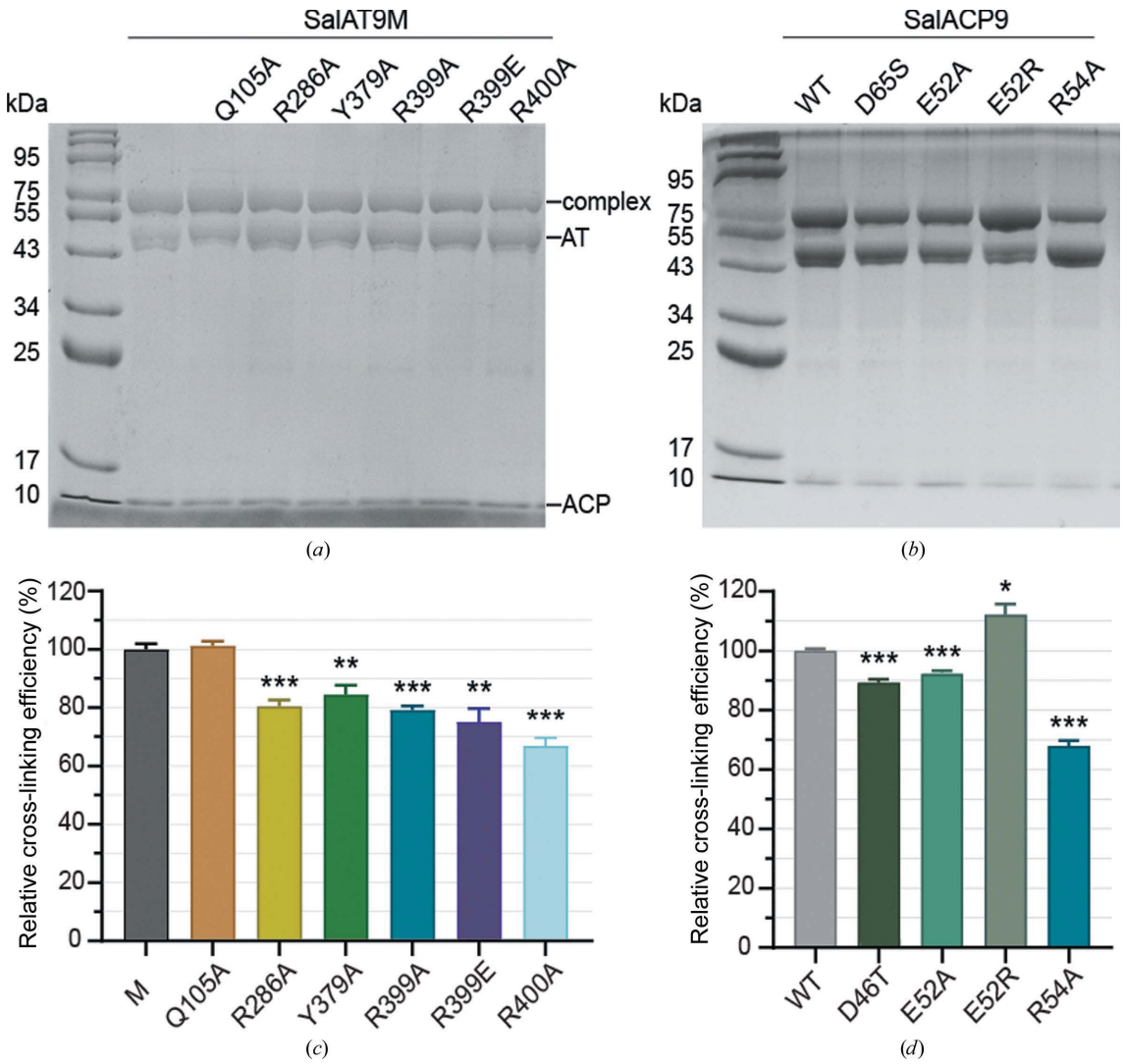

Figure 5
The effects of mutations on AT–ACP cross-linking. (*a*, *c*) Cross-linking reactions of SalAT9 mutants with SalACP9. (*b*, *d*) Cross-linking reactions of SalAT9 with SalACP9 mutants. The cross-linking efficiency was calculated as in Fig. 1. The cross-linking efficiency of the Q105A mutant is the same as that of SalAT9M3. The E52R mutant of SalACP9 showed slightly higher cross-linking efficiency than wild-type ACP. All other mutants showed a reduced cross-linking efficiency. Data are presented as the mean ± SEM from three independent assays. Statistical analyses were performed using the unpaired Student's *t*-test (two-tailed). * $p < 0.05$; ** $p < 0.01$; *** $p < 0.001$.

Arg399 located in loop 12 of SalAT9M is sandwiched between the negatively charged Asp46 of the SalACP9 'DSL' motif and Glu52 located in the middle of the SalAT9M αII helix, and makes bidentate hydrogen bonds to the Glu52 and Asp46 side chains (Fig. 3*d*). Arg399 of SalAT9M and Asp46 and Glu52 of SalACP9 are conserved in mPKSs (Supplementary Figs. S5 and S8), indicating that they may form common important interactions between *cis*-AT and ACP domains. Several other interactions are also observed between the SalAT9 large subdomain and SalACP9. The side chain of Tyr379 of SalAT9M forms hydrogen bonds to Asp55 and Arg54 of SalACP9. Val51 of SalACP9 forms hydrophobic contacts with Try379 of SalAT9M by stacking on top of the aromatic ring. Leu48 of SalACP9 also forms hydrophobic contacts with Tyr379, Pro375 and Arg399 of SalAT9M (Fig. 3*e*).

3.4. The small ferredoxin-like subdomain and KS-to-AT linker constrain ACP binding

The short helix αIII′ of loop II of SalACP9 packs against loop C (residues 284–286) of the small subdomain of SalAT9M (Fig. 4). Ala67 and Thr68 of SalACP9 make hydrophobic contacts with the side chain of Arg286 of SalAT9M, which forms a hydrogen bond to the 4′-phosphopantetheine attached to Ser47 of SalACP9 (Fig. 4*a*). We observed a standalone SalAT9M molecule in the crystallographic asymmetric unit of the complex structure. When the standalone SalAT9M was superposed onto AT in the complex, we noted an obvious movement of the small subdomain, which rotates by 8° on binding SalACP9 (Fig. 4*b*). SalAT9M in the complex structure is in an open state compared with the standalone SalAT9M structure. Dynamics simulations of MonAT5 have previously revealed the movement of the small subdomain relative to the

large subdomain (Bravo-Rodriguez *et al.*, 2014). To confirm whether the movement of the small subdomain is induced by SalACP9 binding, we solved the structure of SalAT9 under different crystallization conditions and found that it is indeed in the expected closed state (Supplementary Fig. S9*a*). The corresponding movement of the small subdomain is also observed when comparing the structures of the VinK–VinL complex and standalone VinK (Supplementary Fig. S9*b*; Miyanaga *et al.*, 2016). In contrast, the binding of DSZS ACP1 to DSZS AT does not induce an obvious conformation change of the small subdomain of DSZS AT (Wong *et al.*, 2011; Miyanaga *et al.*, 2018; Supplementary Fig. S9*c*). The residues of SalAT9M involved in interactions with SalACP9, including Met82, Arg286, Tyr379 and Arg399, show obvious conformational changes upon SalACP9 binding, which are obviously necessary for forming proper protein interactions (Supplementary Fig. S10).

The KS-to-AT linker has been shown to function as a structural element stabilizing AT expressed as a standalone domain. The absence or incompleteness of KS-to-AT linkers in AT constructs may result in insoluble or inactive proteins (Chen *et al.*, 2007). The complex structure shows that loop IV (residues 80–86) of the KS-to-AT linker makes contacts with the N-terminal residues of loop I of SalACP9 (Fig. 4*c*). The backbone NH of Gly85 of SalAT9M makes a hydrogen bond to the backbone carbonyl O atom of Gly27 of SalACP9. Met82 and Pro83 of SalAT9M form hydrophobic contacts with Ala29 of SalACP9 (Fig. 4*d*). Obviously, the KS-to-AT linker and the small subdomain SalAT9 cooperate with each other to sterically constrain the binding of SalACP9 (Fig. 2*b*).

3.5. Mutational analysis

To confirm the importance of the residues at the AT–ACP interface, we introduced mutations into SalAT9M and SalACP9 and carried out cross-linking assays to evaluate their effects on complex formation. Among the SalACP9 residues involved in interactions, Asp46, Glu52 and Arg54 are highly conserved (Supplementary Fig. S8), suggesting that they are all important in AT–ACP recognition, whereas Asp55 is usually an asparagine in other ACPs. We constructed D46T, D46A, E52A, E52R, R54A and D55A mutants of SalACP9, of which the D46A and D55A mutants yielded poorly soluble proteins. No apparent difference in phosphopantetheinyl efficiency was observed between wild-type SalACP9 and the mutants (Supplementary Fig. S11). Similarly, Q105A, R286A, Y379A, R399A, R399E and R400A mutants of SalAT9M were constructed. We evaluated the effects of these mutations by cross-linking SalACP9 mutants with SalAT9M and cross-linking SalAT9M mutants with wild-type SalACP9 (Fig. 5). As expected, the cross-linking efficiency of the Q105A mutant is the same as that of SalAT9M since Gln105 located in the substrate-binding tunnel is not involved in the AT–ACP interaction (Fig. 2*c*). All other mutants showed a reduced cross-linking efficiency, except that the E52R mutant of SalACP9 showed a slightly higher cross-linking efficiency than wild-type ACP (112% $\pm$ 4%).

4. Discussion

During polyketide synthesis, mPKSs utilize ACP domains to shuttle acyl units and growing intermediates among a series of catalytic domains for polyketide chain elongation, modification and termination. Therefore, an ACP domain must interact with each catalytic domain both specifically and reversibly. The inherently weak protein–protein interactions of ACP with its partner catalytic domains are essential for the efficient processivity of mPKSs and should be considered when constructing hybrid mPKSs containing domains from different pathways. However, investigating the weak but important protein–protein interactions is difficult as it requires trapping the transient enzyme–ACP complexes. Burkart and coworkers developed a one-pot cross-linking strategy to capture the transient complexes in fatty-acid synthases and PKSs (Nguyen *et al.*, 2014; Bartholow *et al.*, 2021). In this method, CoA analogs harboring electrophilic warheads that can react irreversibly with the active-site cysteine residues of catalytic domains are synthesized by enzymes of the CoA biosynthetic pathway and are attached to the active-site serine of an ACP domain using a promiscuous phosphopantetheinyl transferase. The crystal structure of the DSZS AT–ACP1 complex was determined using this strategy (Miyanaga *et al.*, 2018). Alternatively, the covalent complex of another *trans*-AT–ACP complex, VinK–VinL, was obtained and structurally characterized using BMOE, a universal cross-linker for conjugation between sulfhydryl groups.

No structure of a *cis*-AT–ACP complex has been reported. In this study, we sought to obtain the SalAT9M–ACP9 complex by using universal maleimide cross-linkers in order to clarify the mechanistic basis of the ACP domain specificity of *cis*-AT domains. The strategy that we used is similar to the VinK–VinL cross-linking experiment. In the VinK–VinL complex structure, a noncatalytic Ser266 located at the base of the substrate-binding tunnel was mutated to a cysteine. The corresponding Asn346 of SalAT9 seems to be less exposed and forms hydrogen bonds to the side chain of Arg215 (Supplementary Fig. S12). We therefore mutated the catalytic Ser190 of SalAT9 to a cysteine. In a previous cross-linking experiment, a DSZS AT mutant in which the catalytic Ser86 is mutated to cysteine could be cross-linked to ACP1, although the yield of the complex was not sufficient for crystallization (Wong *et al.*, 2011). We evaluated several maleimide cross-linkers with different spacer arm lengths and found that BMB had the highest cross-linking efficiency. The 10.9 Å spacer arm length of the BMB cross-linker is longer than that of BMOE (8.0 Å), which was used in cross-linking reactions to obtain the VinK–VinL complex (Fig. 1*c*). The VinK–VinL structure and our SalAT9M–ACP9 structure highlight the potential of bifunctional maleimide reagents in trapping transient complexes of mPKSs for structural characterization since they only require the 4′-phosphopantetheine of the ACP and a cysteine residue at the active site of the partner enzyme. Removing cysteine residues located on the surface of the enzymes may be necessary since they can cause undesired cross-linking reactions (Supplementary Fig. S4*a*).

The SalAT9M–ACP9 structure reveals extensive protein–phosphopantetheine interactions (Supplementary Fig. S13) which differ from those in previously reported AT–ACP structures. In the VinK–VinL structure (Miyanaga *et al.*, 2016), the side chains of Tyr209 and Ser295 form hydrogen bonds to the phosphopantetheine. In the DSZS AT–ACP1 structure (Miyanaga *et al.*, 2018), Gln156 forms a hydrogen bond to the phosphate group, while the Asn150 side chain and the Gln9 backbone make interactions with the arm. Interestingly, more interactions are observed between the arm and the AT in the FabD–AcpP structure (Misson *et al.*, 2020; Supplementary Fig. S13*d*). The different positions and conformations of the arms may affect the ACP-binding modes in the complexes.

The ACP-binding mode of the SalAT9M–ACP9 complex structure is strikingly different from those of *trans*-AT–ACP complex structures. In the structures of both the VinK–VinL (Miyanaga *et al.*, 2016) and DSZS AT–ACP1 (Miyanaga *et al.*, 2018) complexes, the ACP primarily contacts the small domain of the AT, whereas SalACP9 primarily contacts the large subdomain of SalAT9M (Fig. 3). The position of SalACP9 binding is constrained by the KS-to-AT linker and the small subdomain of the AT domain. The orientation of SalAT9M–ACP9 more closely resembles that of VinK–VinL rather than that of DSZS AT–ACP1. When the ATs of the two complex structures are superposed onto each other, the rotation and displacement between SalACP9 and VinL are 12.8° and 9.6 Å, respectively (Supplementary Fig. S14). DSZS AT–ACP1 displays a completely different orientation. The orientation of ACP1 in the DSZS AT—ACP1 complex structure is rotated 130.4° and displaced 6.7 Å from that of SalACP9 in the SalAT9M–ACP9 complex (Supplementary Fig. S14*b*). Both VinL and SalACP9 utilize the αII helix and loop II structure elements to make interactions with AT. In the VinK–VinL complex structure, the αII helix and loop II of VinL pack against the βD strand and the αB helix of the small subdomain of VinK, respectively (Supplementary Fig. S14*d*). The αII helix of VinL contacts VinK by both salt-bridge (between Glu47 of VinL and Arg153 of VinK) and hydrophobic interactions (between Thr39 and Leu43 of VinL and Met206 of VinK; Supplementary Fig. S14*e*). In the SalAT9M–ACP9 complex structure, the αII helix of SalACP9 packs against helix α8 of the large hydrolase subdomain SalAT9M, while loop II of SalACP9 forms interactions with loop C of the small subdomain of SalAT9M (Figs. 3*b* and 4*a*). In the DSZS AT–ACP1 complex structure, the αII helix of DSZS ACP1 forms almost no interactions with DSZS AT except at its N-terminus containing the catalytic Ser46 (Supplementary Fig. S14*f*). Loop II of DSZS ACP1 is placed in a completely different position. The short helix in loop II (αIII′) of DSZS ACP1 packs almost parallelly against the last helix of DSZS AT, which corresponds to helix α8 of SalAT9M. Despite the significantly different ACP-binding mode, the catalytic serine residues of ACPs are positioned at the same position (Supplementary Fig. S14*c*). The reason for the different AT–ACP interaction modes is unclear, but the additional KS-to-AT linker located in the N-terminus of SalAT9M obviously plays important roles in positioning SalACP9 in the complex structure.

Comparison with the AT–ACP of apo Lsd14 reveals different features (Bagde *et al.*, 2021; Supplementary Fig S15). The distance between the catalytic Ser657 of LsdAT7 and Ser1526 of LsdACP7 is 22.5 Å, but this distance is 17.9 Å in the SalAT9M–ACP9 complex. The KS-to-AT linker and the large subdomain act as the major interaction platforms in the apo Lsd14 AT–ACP complex. The small subdomain forms a weak contact with LsdACP7 (Fig. 3*a*). The orientation of LsdACP7 in the Lsd14 complex structure is rotated 54.5° and displaced 8.7 Å from that of SalACP9 in the SalAT–ACP9 complex (Supplementary Fig. S15*e*). LsdACP7 utilizes the αI helix, the αII helix and loop I to contact the αIII helix and loop IV of the KS-to-AT linker of LsdAT7 by hydrogen bonds (between Arg1535 of LsdACP7 and Asp551 and Ala552 of LsdAT7) and salt bridges (between Arg1506 of LsdACP7 and Asp534 of LsdAT7). Similarly, LsdACP7 contacts the α8 helix of the large subdomain of LsdAT7 by the αII helix and loop II. A salt bridge (between Arg1533 of LsdACP7 and Glu845 of LsdAT7) and hydrogen bond (between Arg1543 of LsdACP7 and Gly852 of LsdAT7) act as the major interactions (Supplementary Figs. S15*d* and S15*f*).

The FabD–AcpP complex structure shows the FAS AT–ACP interactions (Misson *et al.*, 2020). In the FabD–AcpP complex structure, AcpP utilizes loop I and the N-terminus of helix II to contact FabD (Supplementary Fig. S15*b*). When the ATs of the two complex structures are superposed onto each other, the rotation and displacement between SalACP9 and AcpP are 119.1° and 5.3 Å, respectively (Supplementary Fig. S15*a*). FabD uses structural elements similar to SalAT9 to contact AcpP. The large subdomain of FabD serves as the major contact platform by using helix α8, strand β6 and loop 10, while the small subdomain utilizes βA, βD and loop C to interact with AcpP.

Protein–protein docking simulations were implemented with *ClusPro* (Kozakov *et al.*, 2017) and *RosettaDock* (Lyskov & Gray, 2008) for SalAT9M and SalACP9. A representative docked model of SalAT9M–ACP9 was obtained and is shown in Supplementary Figure S16. The binding free energy was −2.71 kcal mol^{-1}, which is comparable to that of the SalAT9M–ACP9 crystal structure (−3.44 kcal mol^{-1}). The ACP-binding mode in the docked model also resembles the crystal structure. The large subdomain of SalAT9M acts as the major interaction platform. SalACP9 utilizes helix II to interact with the α8 helix, loop 10 and loop 12 of the SalAT9M large subdomain (Supplementary Fig. S16*b*). The docked SalACP9 shows a slight difference compared with SalACP9 in the crystal structure, showing a rotation and a displacement of 21.7° and 3.3 Å, respectively (Supplementary Fig. S16*c*). These results suggest that the SalAT9M–ACP9 crystal structure is likely to be reasonable.

Typical mPKSs have a *cis*-AT domain in every module to recruit acyl units. The ability of a *cis*-AT to discriminate its cognate ACP partner from other ACP domains of the same enzyme has been noted. However, the detailed *cis*-AT–ACP recognition mechanism is still obscure due to a lack of struc-

tural information. The SalAT9M3–ACP9 complex structure enables the direct visualization of protein–protein interactions between a *cis*-AT and its cognate ACP partner, and helps us to understand previous biochemical analyses that are difficult to understand from sequence comparison. The SalAT9M–ACP9 complex structure shows that loop IV (residues 80–86) of the KS-to-AT linker directly contacts loop I of SalACP9 (Fig. 4*c*), explaining the observation that the core *cis*-AT domain with truncated linker regions displays attenuated activity (Wong *et al.*, 2010). By exchanging segments of different *cis*-ATs, a short C-terminal segment is demonstrated to be the principal determinant of the acyl-CoA specificity of *cis*-ATs (Lau *et al.*, 1999). This segment corresponds to residues 378–423 of SalAT9, containing helix α8 (residues 378–388) and loop 12 (residues 397–404) of the large hydrolase subdomain. These structural elements of SalAT9 form the major binding platform for SalACP9 in the complex structure. Arg399, which makes salt bridges with Asp46 and Glu52 of SalACP9, is also located in this segment (Fig. 3*d*). The ACP specificity of *cis*-AT domains from DEBS has been extensively investigated. For DEBS AT3, a ∼25-fold preference is observed for the cognate ACP3 compared with ACP6 (Dunn *et al.*, 2013). In contrast, the specificity of DEBS AT6 is ∼23-fold higher for ACP6 than for ACP3. To understand the ACP specificity of the two *cis*-ATs, we built DEBS AT6, ACP3 and ACP6 structures using *AlphaFold*2 (Jumper *et al.*, 2021) and adopted the DEBS AT3 structure from the crystal structure of the KS–AT3 didomain of DEBS module 3 (PDB entry 2qo3; Tang *et al.*, 2007). The electrostatic surfaces involved in *cis*-AT–ACP interactions were compared. The most obvious difference is that helix α8 of DEBS AT3 is more negatively charged than that of DEBS AT6. Correspondingly, the αII helix of DEBS ACP3, which recognizes helix α8 of the AT, is more positively charged than that of DEBS ACP6 (Supplementary Fig. S17).

5. Conclusion

In this study, we used BMB as a cross-linking agent to trap the transient AT–ACP complex and structurally characterized the SalAT9M–ACP9 complex of the salinomycin mPKS. The complex structure provides detailed insights into the binding interface between the AT and ACP domains of a *cis*-AT mPKS. The ACP-binding mode in the complex is completely different from those observed in reported *trans*-AT–ACP complexes. The large subdomain of the AT plays the most important roles in recognizing the ACP, while the small subdomain and the KS-to-AT linker cooperate with each other to sterically constrain binding of the ACP. The complex structure is useful in understanding *cis*-AT–ACP recognition and could potentially help to optimize chimeric *cis*-AT mPKSs.

Acknowledgements

We thank beamlines BL18U1 and BL19U1 at Shanghai Synchrotron Radiation Facility for diffraction data collection.

Funding information

This work was supported by National Key R&D Program of China (2020YFA0907900) and National Natural Science Foundation of China (32070040).

References

Alekseyev, V. Y., Liu, C. W., Cane, D. E., Puglisi, J. D. & Khosla, C. (2007). *Protein Sci.* **16**, 2093–2107.
Bagde, S. R., Mathews, I. I., Fromme, J. C. & Kim, C.-Y. (2021). *Science*, **374**, 723–729.
Bartholow, T. G., Sztain, T., Patel, A., Lee, D. J., Young, M. A., Abagyan, R. & Burkart, M. D. (2021). *Commun. Biol.* **4**, 340.
Bravo-Rodriguez, K., Ismail-Ali, A. F., Klopries, S., Kushnir, S., Ismail, S., Fansa, E. K., Wittinghofer, A., Schulz, F. & Sanchez-Garcia, E. (2014). *ChemBioChem*, **15**, 1991–1997.
Bravo-Rodriguez, K., Klopries, S., Koopmans, K. R., Sundermann, U., Yahiaoui, S., Arens, J., Kushnir, S., Schulz, F. & Sanchez-Garcia, E. (2015). *Chem. Biol.* **22**, 1425–1430.
Chen, A. Y., Cane, D. E. & Khosla, C. (2007). *Chem. Biol.* **14**, 784–792.
Cogan, D. P., Zhang, K., Li, X., Li, S., Pintilie, G. D., Roh, S. H., Craik, C. S., Chiu, W. & Khosla, C. (2021). *Science*, **374**, 729–734.
Debreczeni, J. É. & Emsley, P. (2012). *Acta Cryst.* D**68**, 425–430.
Delgado, J., Radusky, L. G., Cianferoni, D. & Serrano, L. (2019). *Bioinformatics*, **35**, 4168–4169.
Dodge, G. J., Maloney, F. P. & Smith, J. L. (2018). *Nat. Prod. Rep.* **35**, 1082–1096.
Dunn, B. J., Cane, D. E. & Khosla, C. (2013). *Biochemistry*, **52**, 1839–1841.
Dunn, B. J., Watts, K. R., Robbins, T., Cane, D. E. & Khosla, C. (2014). *Biochemistry*, **53**, 3796–3806.
Emsley, P., Lohkamp, B., Scott, W. G. & Cowtan, K. (2010). *Acta Cryst.* D**66**, 486–501.
Jiang, C., Wang, H., Kang, Q., Liu, J. & Bai, L. (2012). *Appl. Environ. Microbiol.* **78**, 994–1003.
Jumper, J., Evans, R., Pritzel, A., Green, T., Figurnov, M., Ronneberger, O., Tunyasuvunakool, K., Bates, R., Žídek, A., Potapenko, A., Bridgland, A., Meyer, C., Kohl, S. A. A., Ballard, A. J., Cowie, A., Romera-Paredes, B., Nikolov, S., Jain, R., Adler, J., Back, T., Petersen, S., Reiman, D., Clancy, E., Zielinski, M., Steinegger, M., Pacholska, M., Berghammer, T., Bodenstein, S., Silver, D., Vinyals, O., Senior, A. W., Kavukcuoglu, K., Kohli, P. & Hassabis, D. (2021). *Nature*, **596**, 583–589.
Kalkreuter, E., CroweTipton, J. M., Lowell, A. N., Sherman, D. H. & Williams, G. J. (2019). *J. Am. Chem. Soc.* **141**, 1961–1969.
Klaus, M. & Grininger, M. (2018). *Nat. Prod. Rep.* **35**, 1070–1081.
Koryakina, I., Kasey, C., McArthur, J. B., Lowell, A. N., Chemler, J. A., Li, S., Hansen, D. A., Sherman, D. H. & Williams, G. J. (2017). *ACS Chem. Biol.* **12**, 114–123.
Kosol, S., Jenner, M., Lewandowski, J. R. & Challis, G. L. (2018). *Nat. Prod. Rep.* **35**, 1097–1109.
Kozakov, D., Hall, D. R., Xia, B., Porter, K. A., Padhorny, D., Yueh, C., Beglov, D. & Vajda, S. (2017). *Nat. Protoc.* **12**, 255–278.
Lau, J., Fu, H., Cane, D. E. & Khosla, C. (1999). *Biochemistry*, **38**, 1643–1651.
Li, Y., Zhang, W., Zhang, H., Tian, W., Wu, L., Wang, S., Zheng, M., Zhang, J., Sun, C., Deng, Z., Sun, Y., Qu, X. & Zhou, J. (2018). *Angew. Chem. Int. Ed.* **57**, 5823–5827.
Lyskov, S. & Gray, J. J. (2008). *Nucleic Acids Res.* **36**, W233–W238.
Misson, L. E., Mindrebo, J. T., Davis, T. D., Patel, A., McCammon, J. A., Noel, J. P. & Burkart, M. D. (2020). *Proc. Natl Acad. Sci. USA*, **117**, 24224–24233.
Miyanaga, A., Iwasawa, S., Shinohara, Y., Kudo, F. & Eguchi, T. (2016). *Proc. Natl Acad. Sci. USA*, **113**, 1802–1807.
Miyanaga, A., Ouchi, R., Ishikawa, F., Goto, E., Tanabe, G., Kudo, F. & Eguchi, T. (2018). *J. Am. Chem. Soc.* **140**, 7970–7978.

Murshudov, G. N., Skubák, P., Lebedev, A. A., Pannu, N. S., Steiner, R. A., Nicholls, R. A., Winn, M. D., Long, F. & Vagin, A. A. (2011). *Acta Cryst.* D**67**, 355–367.
Nguyen, C., Haushalter, R. W., Lee, D. J., Markwick, P. R., Bruegger, J., Caldara-Festin, G., Finzel, K., Jackson, D. R., Ishikawa, F., O'Dowd, B., McCammon, J. A., Opella, S. J., Tsai, S. C. & Burkart, M. D. (2014). *Nature*, **505**, 427–431.
Nivina, A., Yuet, K. P., Hsu, J. & Khosla, C. (2019). *Chem. Rev.* **119**, 12524–12547.
Pfeifer, B. A., Admiraal, S. J., Gramajo, H., Cane, D. E. & Khosla, C. (2001). *Science*, **291**, 1790–1792.
Riener, C. K., Kada, G. & Gruber, H. J. (2002). *Anal. Bioanal. Chem.* **373**, 266–276.
Schlee, S., Straub, K., Schwab, T., Kinateder, T., Merkl, R. & Sterner, R. (2019). *Proteins*, **87**, 815–825.
Tang, Y., Chen, A. Y., Kim, C.-Y., Cane, D. E. & Khosla, C. (2007). *Chem. Biol.* **14**, 931–943.
Winn, M. D., Ballard, C. C., Cowtan, K. D., Dodson, E. J., Emsley, P., Evans, P. R., Keegan, R. M., Krissinel, E. B., Leslie, A. G. W., McCoy, A., McNicholas, S. J., Murshudov, G. N., Pannu, N. S., Potterton, E. A., Powell, H. R., Read, R. J., Vagin, A. & Wilson, K. S. (2011). *Acta Cryst.* D**67**, 235–242.
Wong, F. T., Chen, A. Y., Cane, D. E. & Khosla, C. (2010). *Biochemistry*, **49**, 95–102.
Wong, F. T., Jin, X., Mathews, I. I., Cane, D. E. & Khosla, C. (2011). *Biochemistry*, **50**, 6539–6548.
Yuzawa, S., Deng, K., Wang, G., Baidoo, E. E. K., Northen, T. R., Adams, P. D., Katz, L. & Keasling, J. D. (2017). *ACS Synth. Biol.* **6**, 139–147.
Yuzawa, S., Mirsiaghi, M., Jocic, R., Fujii, T., Masson, F., Benites, V. T., Baidoo, E. E. K., Sundstrom, E., Tanjore, D., Pray, T. R., George, A., Davis, R. W., Gladden, J. M., Simmons, B. A., Katz, L. & Keasling, J. D. (2018). *Nat. Commun.* **9**, 4569.
Zhang, F., Ji, H., Ali, I., Deng, Z., Bai, L. & Zheng, J. (2020). *ChemBioChem*, **21**, 1309–1314.
Zhang, F., Shi, T., Ji, H., Ali, I., Huang, S., Deng, Z., Min, Q., Bai, L., Zhao, Y. L. & Zheng, J. (2019). *Biochemistry*, **58**, 2978–2986.